

Stable MHz-repetition-rate passively Q-switched microchip laser frequency doubled by MgO:PPLN

E. Mehner · A. Steinmann · R. Hegenbarth ·
H. Giessen · B. Braun

Received: 14 November 2012 / Accepted: 16 March 2013 / Published online: 12 April 2013
© Springer-Verlag Berlin Heidelberg 2013

Abstract We present an Nd³⁺:YVO₄ microchip laser that is passively Q-switched by a semiconductor saturable absorber mirror. The system generates 520 ps pulses at 1064 nm with 340 mW average output power at up to 2.3 MHz repetition rate. Single longitudinal and transverse mode operation with a peak-to-peak timing jitter less than 1 % is achieved. We discuss the influence of different setup parameters by using numerical simulations of the coupled rate equations and FEM simulations of the thermal management. The infrared light was frequency doubled in an MgO:PPLN crystal with up to 75 % conversion efficiency, which to our knowledge is the highest conversion efficiency that was ever achieved with passively Q-switched microchip lasers.

1 Introduction

The interest in simple and economical laser sources in the near infrared and visible region has grown enormously in recent years. One field of application is time-resolved high-resolution microscopy, in particular STED microscopy [1, 2].

For these applications, visible laser sources with high repetition rates (>1 MHz) are needed to minimize measurement times and to avoid sampling errors. The pulse width should be shorter than 1 ns to achieve good signal-

to-noise ratio. Furthermore, for an infrared (IR) system with moderate peak powers, efficient frequency conversion into the visible spectral range is required to generate two wavelengths for the excitation and the stimulated depletion of the fluorescence markers. In addition, such laser sources with repetition rates in the MHz regime and pulse widths in the range between 10 and 500 ps are also of interest as seed sources for amplifier systems [3].

Mode-locked laser oscillators followed by a pulse picker and regenerative amplifier [4] or cavity-dumped laser oscillators [5] can provide short pulses in the MHz range with pulse energies up to 1 mJ and above. A much simpler, more compact, and more economical approach are passively Q-switched microchip lasers [6–8] followed by nonlinear crystals or fibers for nonlinear frequency conversion. In this paper, a completely passive system without any external frequency stabilization will be presented.

2 Experimental setup

The experimental setup of the passively Q-switched microchip laser followed by a second harmonic generation (SHG) stage is displayed in Fig. 1.

A fiber-coupled laser diode (LD; fiber core diameter: 105 μm, NA = 0.22) which is capable of delivering up to 3 W at 808 nm is used as pump source for the microchip laser. The pump light is collimated with a collimating lens ($f = 35$ mm) and focused into the crystal with an aspheric focusing lens ($f = 18$ mm).

The cavity itself consists of a 245 μm long a-cut YVO₄ crystal doped with 3 at % Neodymium ions, a semiconductor saturable absorber mirror (SESAM) [9], and an output coupling mirror (OC). Nd³⁺:YVO₄ is used as laser active material because of its high absorption coefficient of

E. Mehner (✉) · B. Braun
Georg Simon Ohm University of Applied Sciences Nuremberg,
Keßlerplatz 12, 90489 Nuremberg, Germany
e-mail: eva.mehner@ohm-hochschule.de

E. Mehner · A. Steinmann · R. Hegenbarth · H. Giessen
4th Physics Institute and Research Center SCoPE, University of
Stuttgart, Pfaffenwaldring 57, 70550 Stuttgart, Germany

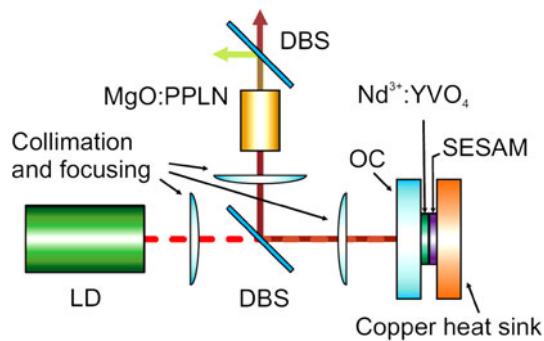


Fig. 1 Experimental setup: passively Q-switched microchip laser pumped by a laser diode (LD), dichroic beam splitter (DBS) for separation of pump and laser radiation, MgO:PPLN for SHG

31.4 cm^{-1} at a wavelength of 808 nm and its high emission cross section of $25 \times 10^{-19} \text{ cm}^2$ of the c -axis at $1,064 \text{ nm}^1$. These parameters are one or two orders of magnitude higher than those of Nd:YAG and Yb:YAG [10] and are necessary for an efficient laser operation despite the short crystal length.

The SESAM exhibits 5 % modulation depth and about 1 ns recovery time. The output coupling mirror is simultaneously used as pump mirror and therefore antireflective coated for the pump wavelength and partially reflective coated ($R = 90 \%$) for the laser wavelength. A dichroic beam splitter (DBS) is used to separate pump and laser radiation.

For second harmonic generation a 10 mm long MgO-doped periodically poled lithium niobate (MgO:PPLN) crystal is used because of its high nonlinear optical coefficient d_{eff} which is about eight times higher than the d_{eff} of bulk beta barium borate.

3 Microchip laser

3.1 Experimental results

In Fig. 2 the average laser power, the pulse duration, and the repetition rate are shown as a function of pump power. As expected, the repetition rate and the average output power at 1,064 nm increase linearly with pump power, whereas the pulse duration and the pulse energy remain nearly constant [11]. Stable laser operation with diffraction limited beam quality can be achieved at up to 0.9 W pump power, which corresponds to 200 mW average output power at 1.1 MHz repetition rate. The optical-to-optical slope efficiency is about 23 %.

The pulse shape was measured with a fast photodiode, which exhibits a rise time of 100 ps (1.2 GHz bandwidth),

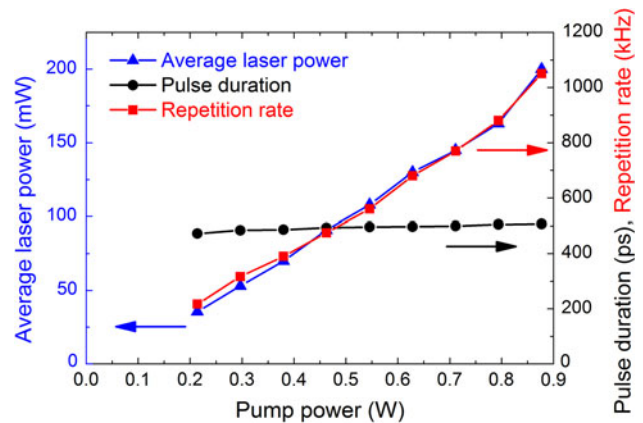


Fig. 2 Pulse duration (circles), repetition rate (squares), and average IR output power (triangles) as a function of pump power of the microchip laser

and is shown in Fig. 3a, indicating 460 ps full width at half maximum (FWHM) pulse duration. The pulse shape is fairly symmetrical.

In the whole displayed pump regime the microchip laser runs at single longitudinal and transverse mode operation.

The spectrum of the microchip laser is displayed in Fig. 4a. It was measured with a spectrometer (ANDO AQ-6315E) which features a spectral resolution of 0.05 nm. As expected, only one longitudinal mode is running, because the mode spacing (1.3 nm) is larger than the gain bandwidth of Nd³⁺:YVO₄ of 0.96 nm FWHM at 1,064 nm. The beam quality M^2 was measured with a SPIRICON M²-200 to be <1.3 up to 0.85 W pump power (Fig. 4b; 11a).

As long as single mode operation is sustained both in longitudinal and transverse directions, the Q-switched pulse train of the laser is very stable. A measurement example for a pulse train at 0.8 W pump power is displayed in Fig. 3b. The peak-to-peak timing jitter is measured with an Agilent 6 GHz Oscilloscope (DSO080604B) and a fast photo diode (Alphaslas UPD-40-VSI-P; rise-time of 40 ps) to be less than 1 % without any additional frequency stabilizing methods which is quite remarkable for a completely passively Q-switched laser source. Using techniques such as injection seeding it has been shown in the past that a further reduction of timing-jitter by several orders of magnitude can be achieved [12].

Theoretical considerations have shown that a smaller pump spot size should support single mode operation at higher pump powers despite the increase of the thermal lens (see Sect. 4). Therefore we changed the focusing lens in our setup from 18 to 15 mm. This results in a pump spot diameter of 45 μm instead of 54 μm . As a consequence we achieved an output power of 340 mW compared to 200 mW. The repetition rate increases linearly up to 2.3 MHz and the pulse width varies between 300 and 520 ps within the entire power range (Fig. 5).

¹ Material specifications by CASIX, Inc.

Fig. 3 Temporal pulse behaviour: **a** pulse shape, **b** pulse train at a pump power of 0.8 W

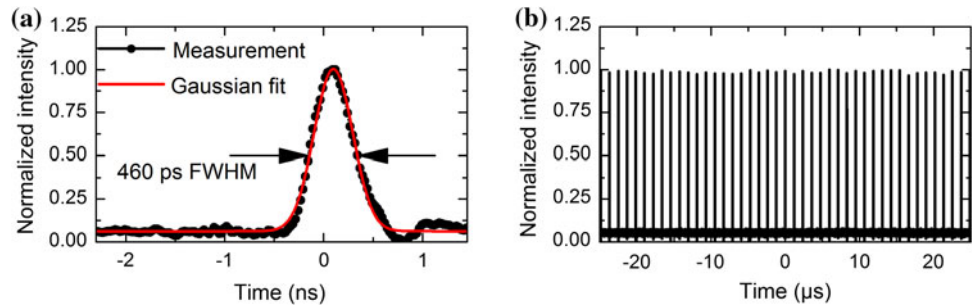


Fig. 4 **a** Spectrum of the microchip laser, **b** beam quality as a function of pump power

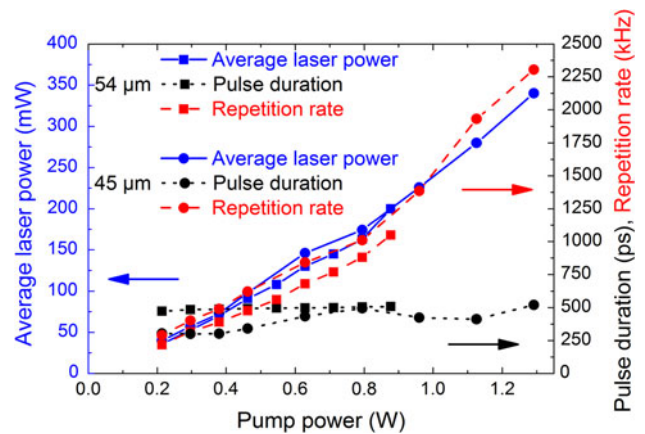
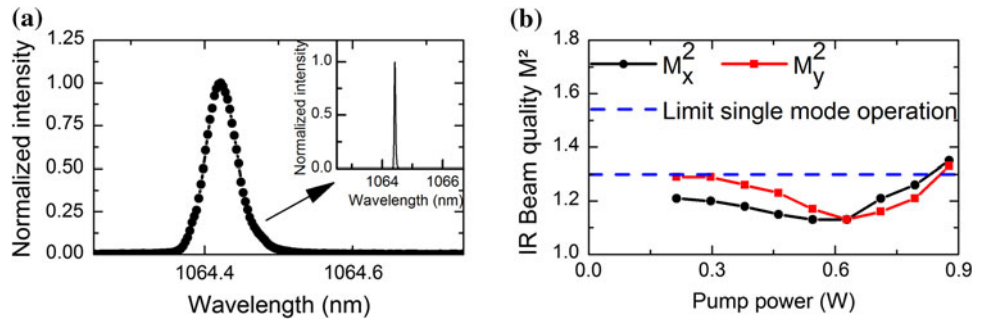


Fig. 5 Pulse duration (black dot), repetition rate (red dash), and average IR output power (blue solid) as a function of pump power of the microchip laser for two different pump spot sizes: 54 μm (squares) and 45 μm (circles)

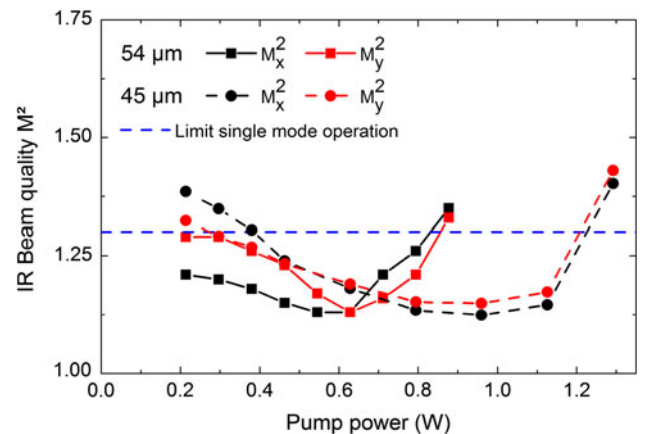


Fig. 6 Beam quality as a function of pump power for two different pump spot sizes: 54 μm (squares-solid) and 45 μm (circles-dash)

Figure 6 demonstrates that the region of stable fundamental mode operation with a M^2 -value below 1.3 becomes broader and is shifted towards higher pump powers. We ascribe the specific dipping of the beam quality in Figs. 4b and 6 to the fact that the best beam quality is achieved for the laser mode roughly being equal or up to 10 % larger than the pump mode. For a laser mode size which is significantly larger than the pump mode, the index profile of the thermal lens induced by the pump beam causes wave front distortions which slightly diminish the beam quality. Once the laser mode is larger than the pump mode higher order modes start to oscillate and the beam quality rapidly gets worse.

3.2 Rate equations: theory and comparison with measurement results

A particular application such as STED microscopy requires a specifically designed laser system. The desired high repetition rates are in conflict with the desired short pulse widths, as can be derived from a zeroth order estimate for the pulse duration τ_{pulse} and the repetition rate f_{rep} [13]:

$$\tau_{\text{pulse}} = \frac{4T_R}{2q_0}, \quad f_{\text{rep}} = \frac{2g_0}{2(2q_0)\tau_L}$$

where T_R is the cavity round-trip time, q_0 is the maximum modulation depth per round-trip with respect to the amplitude, and g_0 is the amplitude small signal gain coefficient per round-trip. τ_L denotes the upper state life time of the laser material. It is clearly visible that a short

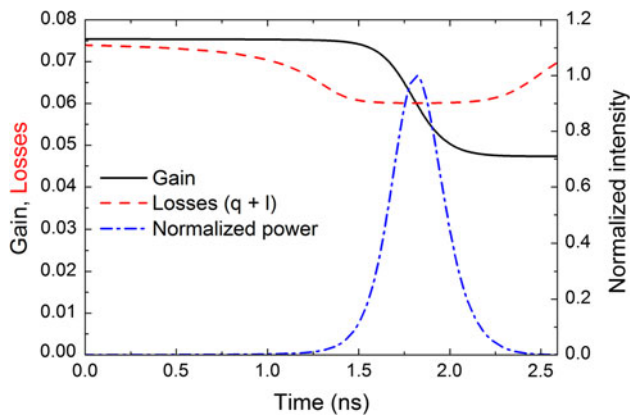


Fig. 7 Pulse formation: normalized power (dash dot), gain (solid), and total losses (dash) as a function of time, q are the saturable losses and l the non-saturable losses including the output coupling

pulse duration requires a high modulation depth, which is in contrast to the desired high repetition rate. Therefore, numerical simulations of the coupled rate equations of the laser power, the losses, and the gain [13] were necessary to determine the required parameter field of the setup (modulation depth of the absorber, crystal properties, and output coupling).

An example for these simulations is shown in Fig. 7. As soon as the gain compensates the total losses of the laser (saturable and non-saturable), the power starts to grow. The increasing photon density bleaches the absorber (the saturable losses), which gives rise to a large excess of the gain over the losses. This leads to an avalanche-like clearing of the inversion and the emission of a high energetic pulse. When the gain coefficient equals the total loss coefficient the maximum of the pulse is reached and the instantaneous power decays exponentially. After the transit of the pulse the saturable losses recover and the gain must be pumped to the new loss level again before the next pulse can be emitted.

These simulations allow us to fit the experimental data and to optimize the laser parameters with respect to output power, pulse width, and repetition rate.

In Fig. 8 we depict the comparison between the experimental results from Sect. 3.1 and the computer simulations. For the simulations the following parameters were used: Crystal thickness $L = 245 \mu\text{m}$ (according to the measurement protocol of the manufacturer), mode radius $w_0 = 34 \mu\text{m}$, modulation depth of SESAM $\Delta R = 2.5 \%$, recovery time $\tau_A = 1 \text{ ns}$, saturation fluence $e_{\text{sat}} = 0.35 \text{ J/m}^2$, and output coupling $T = 10 \%$.

For the simulations we used two different values for the additional (non-saturable) losses, namely 1 and 4 %. The simulation with 4 % additional losses fits very well our measurement, which is an indication that there are still more losses within the cavity apart from the absorber and the output coupler.

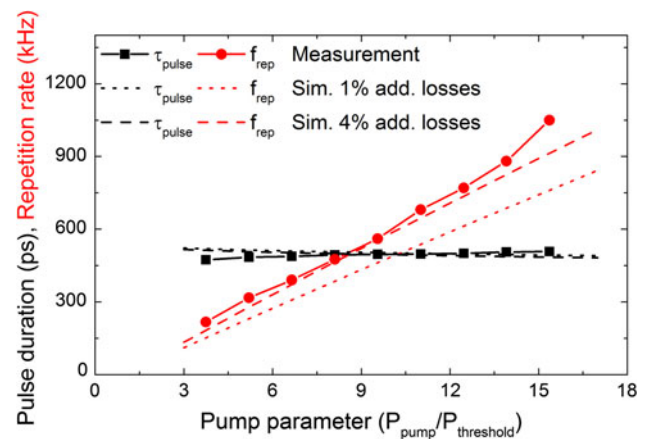


Fig. 8 Repetition rate (red) and pulse duration (black) as a function of the pump parameter (ratio of pump power to threshold power): comparison of measurement and simulation (Sim.)

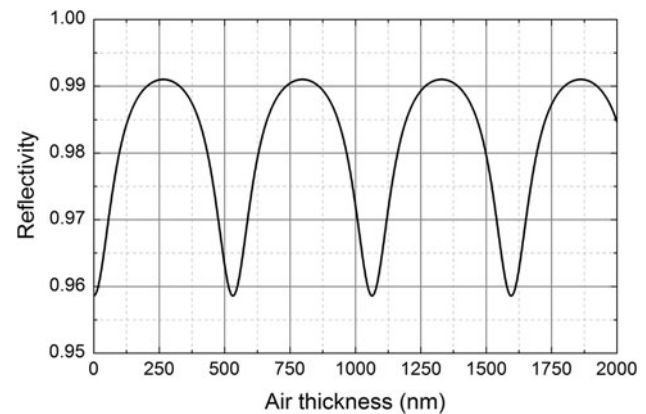


Fig. 9 Low-intensity reflectivity of the absorber as a function of air thickness between absorber and crystal (simulation). The air gap acts as a Fabry–Perot cavity

To fit the pulse width, we used an effective modulation depth of $\Delta R = 2.5 \%$ instead of a specified value of 5 % for the simulations. This has two reasons: The coating of the absorber is not 100 % highly reflective for the continuous wave pump radiation. Therefore, the pump radiation pre-saturates the absorber. Secondly, an air layer between the laser crystal and the SESAM can decrease the effective modulation depth. Unless the laser crystal and the SESAM are not directly bonded with an index matching fluid, the air gap in between is a crucial parameter for the performance. As indicated in Fig. 9, the air gap between the SESAM and the crystal acts as a Fabry–Perot cavity, which leads to a change of the low-intensity reflectivity and therefore to a change of the effective modulation depth as a function of the air gap distance.

Furthermore, in Fig. 10 the pulse width is displayed for different modulation depths. The modulation depth affects not only the pulse width, but also the pulse shape of the

microchip laser. Once the modulation depth is larger than the non-saturable losses, the pulse shape becomes asymmetrical with a longer trailing edge.

3.3 Stability

The microchip cavity presented in our setup consists of two plane mirrors. In this case a thermal lens has to be induced by pumping the active medium to ensure stable laser operation: pumping the active medium (absorption of heat within the crystal) induces a temperature profile which leads to a refractive index profile via the dn/dT -parameter of the material. This refractive index profile acts similar to a GRIN lens, which gives rise for the resonator stability of the microchip laser [14, 15]. Additionally it has been shown that gain-guiding and gain-related index guiding effects contribute to the mode size and thus the laser stability [16].

A stronger thermal lens induces a smaller mode diameter. If the mode diameter becomes smaller than the pump diameter, higher order modes will start to oscillate. Therefore the thermal management and the design of the thermal lens are essential for scaling to larger output powers with diffraction limited beam quality.

Above 0.9 W pump power higher order modes are generated, addicted to the results of the first part of Sect. 3.1. In Fig. 11b these higher order modes are revealed as a dip in the TEM-mode profile of the focused laser beam.

The transverse mode profile at higher pump power (>0.9 W) indicates a superposition of a Gaussian fundamental mode and a higher order mode (TEM_{01*}). This is in full agreement with continuous-wave measurements, where a “donut-mode” has already been observed at lower pump powers. The reason for this behaviour is the better heat conductivity of the SESAM compared to the dielectric highly reflective (HR) mirror and secondly due to the soft aperture effect of the saturable absorber (the lower intensities at the wings experience higher losses).

By increasing the pump power above 0.9 W, we also recognized an increased timing jitter. This is a typical behaviour if multiple longitudinal or transversal modes are oscillating.

It is important to force the laser source towards single longitudinal and single transverse mode operation to ensure stable laser operation. Therefore, one needs an appropriate ratio of absorbed pump power (doping, pump spot size) and heat management (heat conductivity, change of the

Fig. 10 Simulation: pulse width for different modulation depths ΔR : **a** linear and **b** logarithmic display

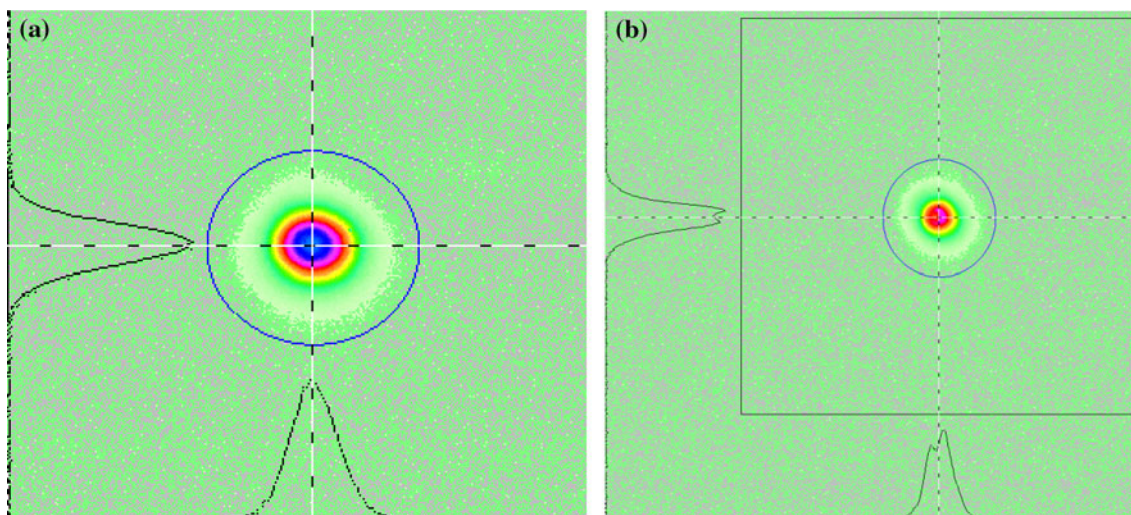
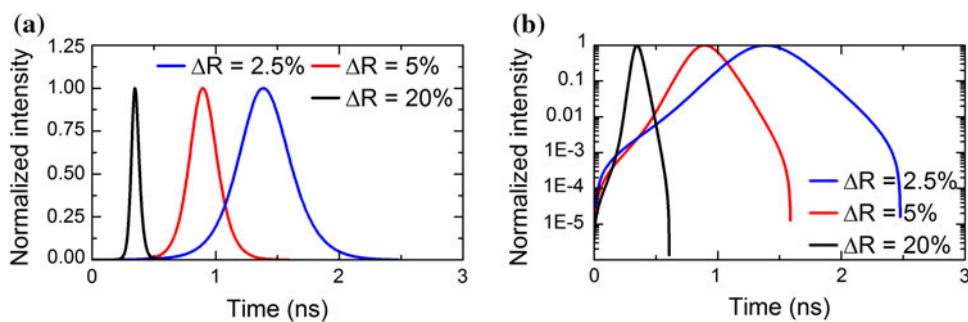


Fig. 11 **a** TEM₀₀-beam profile up to 0.9 W pump power, **b** transverse mode profile at a pump power >0.9 W at 1064 nm: superposition of a TEM₀₀-mode and a TEM_{01*}-mode

refractive indices dn/dT of the active medium, and heat conduction of the end faces).

3.4 FEM simulations of the thermal lens

3.4.1 Theory

As described above, for stable laser operation it is essential to control the strength of the thermal lens. Therefore finite elements methods (FEM) simulations and optimization were carried out for our microchip laser cavity. The simulations were performed for different optical components and different operation regimes (continuous wave operation (cw) with a dielectric HR end mirror, as well as for pulsed laser operation with a semiconductor saturable absorber instead).

In a first step, these different setup models were constructed in the CAD program “ProEngineer Wildfire 4.0”. The influence of different coatings was included by the use of different interface conditions. In a second step, these models were inserted to “Ansys”—a program for heat simulation, see Fig. 12 bottom. The challenge of these simulations is an optimized crosslinking.

As a result the FEM simulations provide longitudinal and radial temperature profiles (see top of Fig. 12). To determine the magnitude of the thermal lens, different radial temperature profiles were extracted at different positions within the laser crystal. The radial temperature profiles were then fitted to a parabolic function. The coefficient of the parabolic term is directly proportional to the temperature dependent nonlinear refractive index n_2 in the quadratic form $n(r) = n(0) - \frac{1}{2}n_2r^2$. These quadratic transverse variations of the thermal lens at different positions within the crystal form different Gaussian ducts which can finally be used to calculate the beam caustic by using the ABCD matrix formalism. By comparing this caustic with the caustic of a plane–plane cavity including a discrete thermal lens in the centre of the resonator, it is possible to determine the magnitude of the overall thermal lens.

To validate the FEM simulations, the two dimensional heat equation for a cylindrical beam profile was solved analytically. A parabolic temperature profile within the pump spot area and a logarithmic decrease outside the pumping region follow from this approximation. In Fig. 15 it can be seen that the analytical solutions and the FEM simulations are in good agreement for a 200 μm long crystal.

3.4.2 Discussion

The primary goal of an optimized heat management is to realize a stable resonator and to match the pump radius

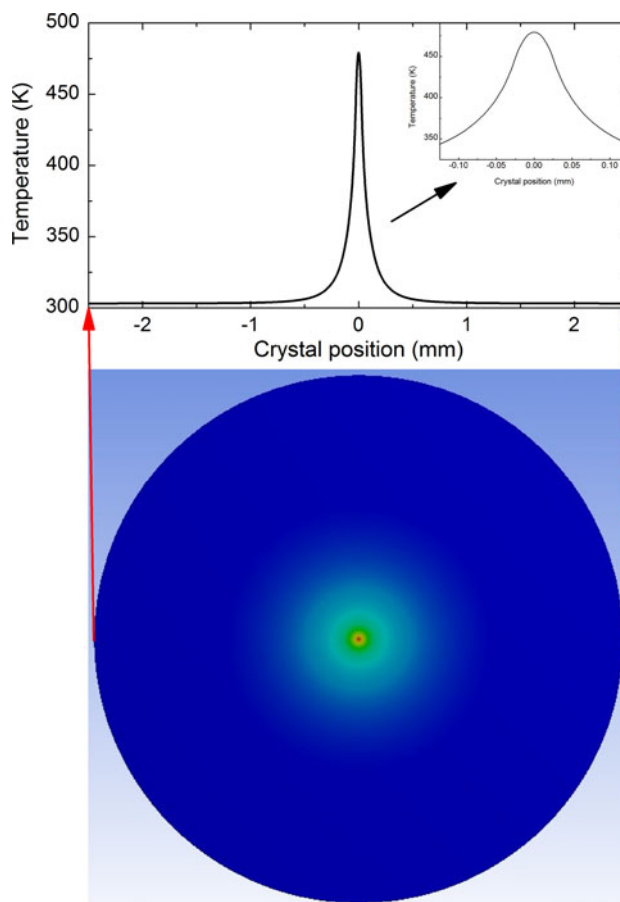


Fig. 12 Simulated heat distribution within the laser crystal: lighter colours correspond to higher temperatures. Top radial temperature profile inside the crystal as a function of the crystal radius in mm

with the laser mode radius. The effective focal length of the thermal lens is quadratically proportional to the pump radius r_p ($f_{\text{therm}} \propto r_p^2$). On the other hand this thermal lens defines the size of the laser beam radius w_L with $w_L \propto \sqrt[4]{f_{\text{therm}}}$. Therefore the laser mode radius w_L is proportional to the square root of the pump radius (via the thermal lens), which yields the surprising result that a smaller pump radius should allow higher pump powers up to the point, where the thermal lens induces a smaller laser mode compared to the pump radius (and higher order modes start to oscillate). In Fig. 13 the mode radius is plotted as a function of the pump radius. Above the red line the laser mode radius is larger than the pump radius and therefore a fundamental TEM_{00} mode is possible—provided that the radial heat flow is still valid and the intensity is below the damage threshold.

The effective focal length of the thermal lens was derived to be in the range of 10–200 mm, depending on the pump spot size, pump power, and the doping level of the laser crystal. This simulation is in good agreement with the recalculated focal length of the microchip laser using the

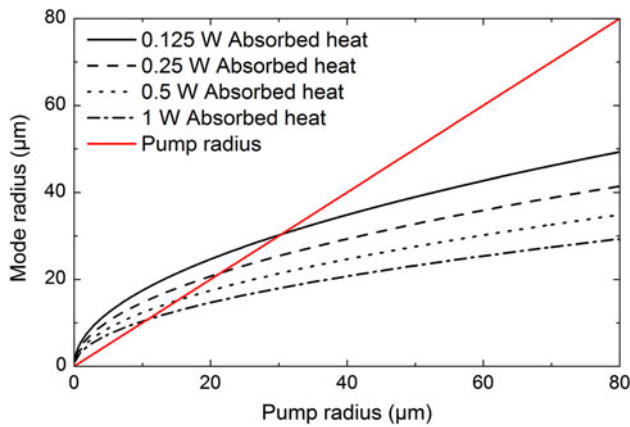


Fig. 13 Mode radius as a function of pump radius for different pump powers (absorbed heat)

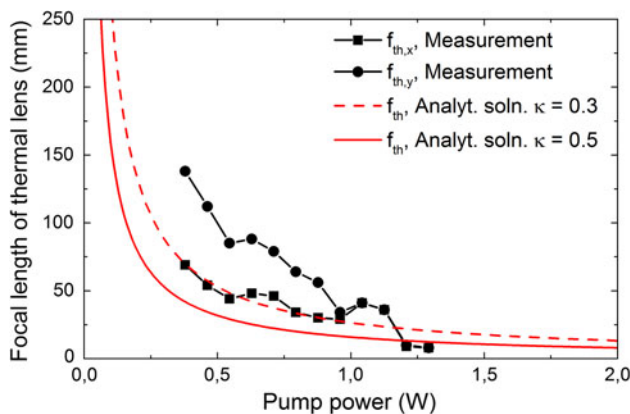


Fig. 14 Effective focal length of the thermal lens as a function of pump power—cw-measurement, comparison with 2D cylindrical analytical solution (Analyt. soln.)

measured beam parameters outside the cavity, as can be seen in Fig. 14. The parameter κ is defined as the ratio of inserted heat to the pump power: $Q = \kappa \cdot P_{\text{pump}}$.

The difference between the two perpendicular directions (x and y) is due to the anisotropic properties of the $\text{Nd}^{3+}:\text{YVO}_4$ crystal. For these experiments an a -cut crystal was used. Therefore there exist two different crystal axes in radial direction—an a -axis and a c -axis—with different thermal properties.

The effective focal length of the thermal lens as a function of the induced heat is shown in Fig. 15. The magnitude of the induced heat is not precisely known. According to Fig. 14 we assume that one third of the pump power is converted to heat within the laser crystal.

For a 200 μm long microchip laser crystal the analytical 2D calculation and the FEM simulation do not differ very much. This changes when shorter crystals are used as will be shown in the following. Additionally, the influence of a partially reflective coating (8 pairs of SiO_2 –

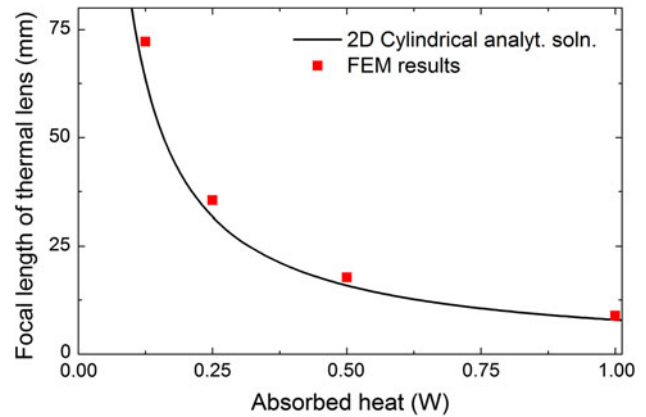


Fig. 15 Focal length of the thermal lens as a function of absorbed heat: comparison of FEM simulation results and 2D cylindrical analytical solution

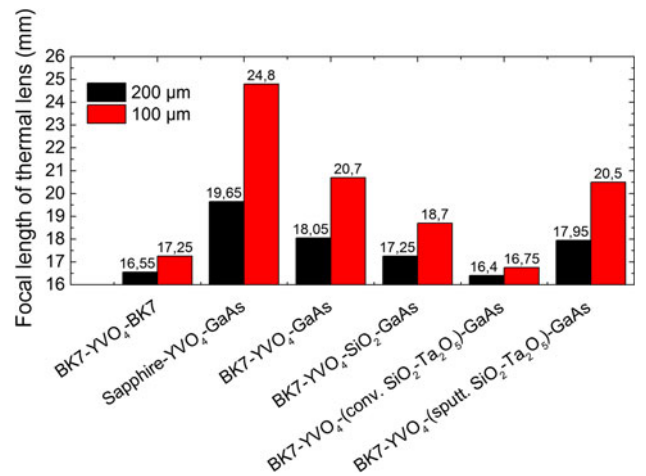


Fig. 16 Different setup configurations for different output couplers and different coatings on top of the SESAM: effective focal length at 0.5 W absorbed heat

Ta_2O_5 with a total physical thickness of 2.45 μm) and different coating processes (conventional or sputtered) on top of the SESAM are examined. As output coupler either a BK7-glas substrate (BK7) or a sapphire substrate (Sapphire) is used. In comparison to the Q-switched microchip laser a laser setup with two BK7-end mirrors is shown. In Fig. 16 the resulting effective focal lengths are plotted for a 200 μm crystal (black) and for a 100 μm long crystal (red).

The differences of the particular setups are quite large. It is shown that the coating and the coating process (conventional or sputtered) have an important influence on the heat management and hence on the focal length of the thermal lens. The use of a sapphire output coupler instead of a BK7 output coupler for example will improve the

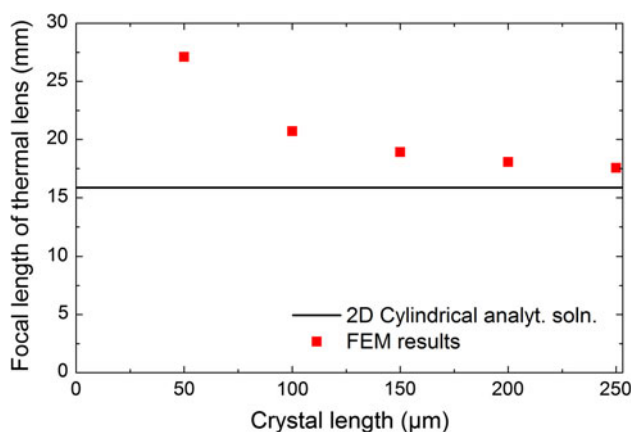


Fig. 17 Focal length of the thermal lens as a function of crystal length at 0.5 W absorbed heat

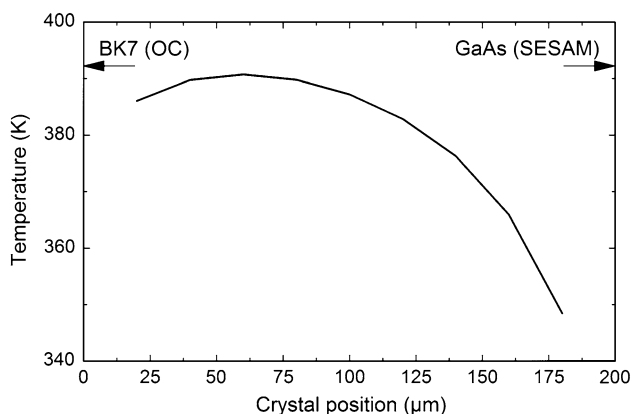


Fig. 18 Longitudinal temperature profile in the center of a 200 μm crystal at 0.25 W absorbed heat

thermal management and allows higher output power while having stable laser operation.

In Fig. 17 the effective focal length of the thermal lens for different crystal lengths is shown. The analytical calculation agrees quite well with the FEM simulation for a 200 μm long crystal. For shorter crystals a heat flow in longitudinal direction can no longer be neglected, and a full 3D FEM model has to be calculated to deduce the optimal thermal properties. Furthermore, the crystal length affects the strength of the thermal lens. Using longer crystals the thermal flow is merely in radial direction and the focal length of the thermal lens becomes shorter.

The heat conduction towards the output coupling mirror and towards the SESAM differ from each other. An example for a longitudinal temperature profile is shown in Fig. 18.

To take this into account we fitted the temperature profile at different positions within the crystals and then calculated a total roundtrip matrix by multiplying different Gaussian ducts.

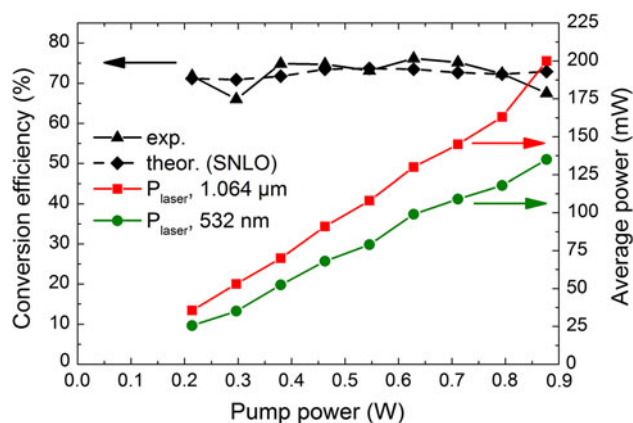


Fig. 19 SHG conversion efficiency, and average IR and green output power as a function of pump power using a 10 mm long MgO:PPLN. The IR power at 1.064 μm was measured before frequency doubling

4 Second harmonic generation

Due to the moderate peak power of the microchip laser (≈ 400 W), a long nonlinear crystal with a high nonlinear optical coefficient d_{eff} is required to achieve high conversion efficiency. Periodically poled lithium niobate has a d_{eff} of about 16 pm/V which is 8-times higher than the d_{eff} of beta barium borate. For a long interaction length a 10 mm long PPLN crystal is used. A small spot of about 80 μm diameter within the PPLN is needed to achieve high intensities, which are necessary for efficient frequency conversion. Therefore, the optimum Rayleigh range of the focused IR beam has to be chosen.

Apart from the smaller nonlinear optical coefficient, the BBO crystal in addition possesses a large walk-off-angle of about 56 mrad. Hence, by using a 10 mm or even longer BBO crystal one would obtain a strongly elliptical beam, which is undesired for applications. For these reasons, a MgO:PPLN crystal is used with a grating period of 6.96 μm at 33 $^{\circ}\text{C}$.

We achieved up to 135 mW average SHG power at 200 mW infrared power, in spite of the moderate infrared peak power of the microchip laser, resulting in a conversion efficiency of 68 %. Over the whole pump power range the conversion efficiency varies only slightly between 68 and 75 % (see Fig. 19) due to the constant peak power (pulse energy and pulse width). Simulations of the efficiencies were carried out with SNLO and correspond well with our measurement results.

5 Conclusion

We presented a microchip laser that was passively Q-switched by a semiconductor saturable absorber mirror. The system generates 520 ps pulses at 1,064 nm

wavelength with repetition rates up to 2.3 MHz at 340 mW average output power. Stable laser operation of the microchip laser was achieved without any external frequency stabilization. We showed that the measurement results fit well to the expected simulation results by numerical simulation of the coupled rate equations. We discussed different aspects of the stability of the system, such as rate equation analysis and FEM simulation of the thermal lens. With a 10 mm long MgO:PPLN crystal a SHG conversion efficiency of 75 % was demonstrated, leading up to 135 mW of 1.1 MHz subnanosecond pulses at 532 nm.

Acknowledgments We acknowledge Jochen Bönig and Andreas Dietz for performing the FEM simulations. This research project is financially supported by the German Federal Ministry of Education and Research (No.: 17 N 43 08).

References

1. T.A. Klar, S. Jakobs, M. Dyba, A. Egner, S.W. Hell, Fluorescence microscopy with diffraction resolution barrier broken by stimulated emission. *Proceedings of the National Academy of Sciences* **97**, 8206–8210 (2000)
2. B.R. Rankin, R.R. Kellner, S.W. Hell, Stimulated-emission-depletion microscopy with a multicolor stimulated-Raman-scattering light source. *Optics Letters* **33**, 2491–2493 (2008)
3. A. Steinmetz, F. Jansen, F. Stutzki, R. Lehneis, J. Limpert, A. Tünnermann, Sub-5-ps, multimegawatt peak-power pulses from a fiber-amplified and optically compressed passively Q-switched microchip laser. *Optics Letters* **37**, 2550–2552 (2012)
4. C. Hönninger, R. Paschotta, M. Graf, F. Morier-Genoud, G. Zhang, M. Moser, S. Biswal, J. Nees, A. Braun, G.A. Mourou, I. Johannsen, A. Giesen, W. Seeber, U. Keller, Ultrafast ytterbium-doped bulk lasers and laser amplifier. *Appl. Phys. B* **69**, 3–17 (1999)
5. A. Killi, A. Steinmann, J. Döring, U. Morgner, M.J. Lederer, D. Kopf, C. Fallnich, High-peak-power pulses from a cavity-dumped Yb:KY(KW₄)₂ oscillator. *Optics Letters* **30**, 1891–1893 (2005)
6. J.J. Zayhowski, C. Dill III, Diode-pumped passively Q-switched picosecond microchip lasers. *Optics Letters* **19**, 1427–1429 (1994)
7. B. Braun, F.X. Kärtner, G. Zhang, M. Moser, U. Keller, 56-ps passively Q-switched diode-pumped microchip laser. *Optics Letters* **22**, 381–383 (1997)
8. A. Steinmetz, D. Nodop, J. Limpert, R. Hohmuth, W. Richter, A. Tünnermann, 2 MHz repetition rate, 200 ps pulse duration from a monolithic, passively Q-switched microchip laser. *Appl. Phys. B* **97**, 317–320 (2009)
9. U. Keller, K.J. Weingarten, F.X. Kärtner, D. Kopf, B. Braun, I.D. Jung, R. Fluck, C. Hönninger, N. Matuschek, J. Aus der Au, Semiconductor saturable absorber mirrors (SESAM's) for femtosecond to nanosecond pulse generation in solid-state lasers. *IEEE Journal of Selected Topics in Quantum Electronics* **2**, 435–453 (1996)
10. Material specifications by GWU-Lasertechnik: <http://www.gwu-group.de/cmslaser/>
11. G.J. Spühler, R. Paschotta, R. Fluck, B. Braun, M. Moser, G. Zhang, E. Gini, U. Keller, Experimentally confirmed design guidelines for passively Q-switched microchip lasers using semiconductor saturable absorbers. *J. Opt. Soc. Am. B* **16**, 376–388 (1999)
12. A. Steinmetz, D. Nodop, A. Martin, J. Limpert, A. Tünnermann, Reduction of timing jitter in passively Q-switched microchip lasers using self-injection seeding. *Optics Letters* **35**, 2885–2887 (2010)
13. B. Braun, Compact pulsed diode-pumped solid-state lasers, Diss., ETH No: 11953, 1996
14. J. J. Zayhowski, in *Thermal guiding in Microchip lasers*, ed. by H. P. Jenssen and G. Dubé. *Advanced solid-state lasers*, vol. 5 (Washington, DC, 1990): Opt. Soc. America, OSA Proc. Series, 9–13
15. R.S. Conroy, *Microchip lasers*, Dissertation, University of St. Andrews, 1998
16. A.J. Kemp, R.S. Conroy, G.J. Friel, B.D. Sinclair, Guiding effects in Nd:YVO₄ microchip lasers operating well above threshold. *IEEE Journal of Quantum Electronics* **35**, 675–681 (1999)